THE ASTROPHYSICAL JOURNAL, 535:501–511, 2000 May 20

MID-INFRARED OBSERVING CONDITIONS AT THE SOUTH POLE

M. A. CHAMBERLAIN, M. C. B. ASHLEY, M. G. BURTON, A. PHILLIPS, AND J. W. V. STOREY
Joint Australian Centre for Astrophysical Research in Antarctica (JACARA), School of Physics, University of New South Wales, Sydney 2052, Australia; m.burton@unsw.edu.au

AND

D. A. HARPER
University of Chicago, Yerkes Observatory, Williams Bay, Wisconsin 53191
Received 1999 September 22; accepted 1999 December 20

ABSTRACT

Measurements of the mid-infrared sky brightness at the South Pole throughout the winter of 1998 show that the sky background is extremely low and stable. For 50% of the time, the flux in the 8.78 to 9.09 μm window is below 50 Jy per square arcsecond. Typical background levels in this window during clear conditions are of the order of 20 Jy per square arcsecond. This is almost an order of magnitude better than any other site on earth. The lower limit to the sky background across most of the N window appears to be set by the aerosol content of the sky rather than by residual water vapor. These data were acquired remotely using an automated instrument housed in the AASTO (Automated Astrophysical Site-Testing Observatory).

Subject headings: atmospheric effects — infrared: general — site testing

1. INTRODUCTION

Astronomical observations in the mid-infrared from the ground are limited by an atmospheric thermal background flux that is orders of magnitude greater than that of the objects studied. The difficulties faced are most eloquently described by Low & Rieke (1974): "Observing at 10 μm has been likened to observing visually through a telescope lined with luminescent panels and surrounded by flickering lights as though the telescope dome were on fire."

So dominant is the local thermal background that any improvement in site quality will translate directly into improved sensitivity for astronomical observations. The most important parameters affecting the quality of a site are atmospheric temperature, stability, and water-vapor content.

The antarctic plateau promises significant advantages for astronomy in the thermal infrared; that is, for wavelengths greater than about 2.3 μm. The high-altitude, low water-vapor content, cold atmosphere, and the stable air mass has the potential to provide conditions that are superior to any other ground-based site. In the "K-dark" window (2.3–2.4 μm), the low temperature provides a dramatic decrease in the background radiation. Near-infrared wavelengths are on the Wien side of the Planck function at atmospheric temperatures, with the result that radiation is extremely sensitive to changes in temperature. Measurements made at the South Pole in the K-dark window show reductions in background flux, relative to that at temperate sites, by factors of between 10 and 100 (Ashley et al. 1996; Nguyen et al. 1996; Phillips et al. 1999).

In the L window (2.9–4.2 μm), the background flux is typically 20 times lower than that at temperate sites (Ashley et al. 1996; Phillips et al. 1999). A preliminary exploration of the benefits this confers to wide-field thermal infrared imaging is currently being conducted with the SPIREX/Abu experiment, a 60 cm telescope equipped with a 1024 × 1024 pixel InSb array camera (Fowler et al. 1998).

Terrestrial thermal emission peaks in the mid-infrared, so the emission from the sky is not as sensitive to changes in temperature. At the South Pole, calculations show that the lower temperatures should be responsible for a reduction of only a factor of about 2. However, larger reductions in the mid-infrared could result from the decrease in the water-vapor content of the atmosphere, producing lower emissivity. Summer observations of the thermal emission of the atmosphere over the South Pole in the mid-infrared have been reported already by Smith & Harper (1998) and show a greater than expected decrease in sky background.

This paper reports measurements of the mid-infrared sky brightness at the South Pole taken throughout the winter of 1998. The results confirm that the typical sky background is exceptionally low, suggesting that the benefits already seen in the near-infrared will extend across the infrared spectrum.

2. METHOD

2.1. *Instrument*

Results presented here were recorded with the Mid-Infrared Sky Monitor (MISM). A detailed description of this instrument appears in Storey et al. (1999); only a brief overview of its operation will be given here.

The MISM detects the difference in the flux received between two beams, each 4° wide and 45° apart in the sky. A reflective chopper chops between these beams at a frequency of 1kHz. After passing through a filter wheel, the beam is incident on a HgCdTe detector maintained at 77 K by a Stirling-cycle microcooler. The elevation of the two beams can be rotated in a plane from one horizon to the other, passing through zenith. For calibration, a blackbody is placed in the path of one of the beams. The temperature of this blackbody is around -30°C (i.e., approximately 30° above ambient) and is accurately recorded with a platinum resistance thermometer.

The MISM filter wheel contains the following filters:

1. a standard astronomical "N" filter (8.07–13.3 μm),
2. a circular variable filter (CVF) covering 4.3–7.7 μm at a resolving power of $\lambda/\Delta\lambda = 74$,

TABLE 1

TYPICAL OPERATING SEQUENCE FOR THE MISM—SKYDIPS

Wavelength (μm)	Comments
8–13	N window
10.6–11.3	N-dark window
14.0	Carbon dioxide emission
9.8	Ozone emission
7.8	Water emission

3. a CVF covering 7.7–14.1 μm at $\lambda/\Delta\lambda = 55$, and
4. a narrowband filter covering 10.6–11.3 μm, allowing sensitive measurements to be made in this region of particularly low sky brightness reported by Smith & Harper (1998).

To facilitate a broad campaign of site testing across a wide range of wavelengths and at a variety of high-plateau antarctic sites, an Automated Astrophysical Site-Testing Observatory (AASTO) has been developed (Storey, Ashley, & Burton 1996; Storey 1998). The AASTO is a self-heated, self-powered, autonomous laboratory that hosts a suite of instruments, each designed to provide data on a particular characteristic of the atmosphere of relevance to astronomy.

The MISM was installed in the AASTO at the South Pole in 1997 January. Difficulties with the thermal generator and power supply of the AASTO meant that no results were obtained with the instrument in the winter of 1997. Over the antarctic summer of 1997–1998, the AASTO was brought back into operation, allowing the MISM to be operated remotely over the antarctic winter of 1998 via telnet sessions from Sydney. Commands for the rotator, filter wheel, integration times, and power and amplifier settings are included in software macros. Data are recorded in two modes: skydips at fixed filter positions and spectra across the CVFs. These are described below.

Skydips are recorded by moving the rotator so that the instrument scans from one horizon to the other, passing through zenith. They are calibrated using the readings obtained when one of the beams passes across the calibration blackbody. Each reading is integrated over 0.3 s. The angle between readings is either 1°.0 or 0°.5; i.e., four or eight times smaller than the resolution of the beam. Skydips are taken with a fixed position on the filter wheel—either through a broadband filter or at a position on the CVF corresponding to the wavelength of a major emission feature of a specific atmospheric constituent, namely, carbon dioxide, ozone, or water.

Spectra are recorded by holding the rotator at a fixed zenith angle and scanning through the full range of the CVF. Readings are integrated over 0.24 or 0.50 s, with the longer integration needed for the 4–8 μm CVF because of lower signal levels. Step sizes on the filter of $\triangle\lambda = 0.018$ μm and $\triangle\lambda = 0.010$ μm are used for the 4–8 and the 8–14 μm CVFs, respectively. The absolute sky flux is derived from the differential readings by combining the results from appropriate rotator positions (see § 3). Knowing the flux from the calibration blackbody and assuming a ratio between the flux at the zenith and that at 45°, the zenith flux can be calculated.

Tables 1 and 2 show a typical operation sequence for the MISM.

3. THEORY

Thermal emission from the atmosphere in the mid-infrared can be modeled by assuming that the emission comes from a single, flat, emissive layer at a uniform temperature. Under this assumption, the variation in downwelling radiation with zenith angle is determined solely by the optical path length at the angle viewed, which is proportional to the secant of the zenith angle. By converting the optical depth into emissivity, the following relation between flux (F_λ) and angle (θ) can be found:

$$F_\lambda(\theta) = A_\lambda(1 - e^{-\tau_\lambda \sec \theta}) , \quad (1)$$

where A_λ is the flux from a blackbody at the atmospheric temperature, τ_λ is the optical thickness of the layer through zenith, and θ is the angle of the beam from zenith.

This expression can be modified to model the signal from the MISM, which detects the difference in flux received by two beams 45° apart in zenith angle. The modified expression is written in terms of θ, which we now take to be the zenith angle halfway between the two beams. We will also write zenith angles to one side of the zenith (counterclockwise rotator position as viewed by the detector) as negative and to the other side as positive. The zenith angle of the two beams is then $(\theta - 22.^\circ5)$ and $(\theta + 22.^\circ5)$. The equation for the differential flux can then be written:

$$\begin{aligned} \triangle F(\theta) &= F(\theta + 22.5) - F(\theta - 22.5) \\ &= A[e^{-\tau \sec (\theta - 22.5)} - e^{-\tau \sec (\theta + 22.5)}] . \end{aligned} \quad (2)$$

This relation, where we have dropped the subscript λ for convenience, has been used to create the theoretical skydips shown in Figure 1. The different curves demonstrate the effect of different values of optical depth. The blackbody flux (A) has been set to unity for all of these curves. For small τ, the skydip curves show a clear S-shape about the zenith position. However, as τ increases, the curves reach a maximum at some particular zenith angle and then turn over.

When τ is not too small, curve-fitting to the detailed shape of the skydip can give both the flux and the differential optical thickness. Equation (1) can then be used to cal-

TABLE 2

TYPICAL OPERATING SEQUENCE FOR THE MISM—SPECTRA

Rotator Position (deg)	Zenith Angle[a] of Beam 1 (deg)	Zenith Angle of Beam 2 (deg)
−22.5	−45	0 (zenith)
22.5	0	45
0	−22.5	22.5
67.5	45	90 (blackbody calibrator)

[a] Zenith angles are written as positive on one side of the zenith and negative on the other.

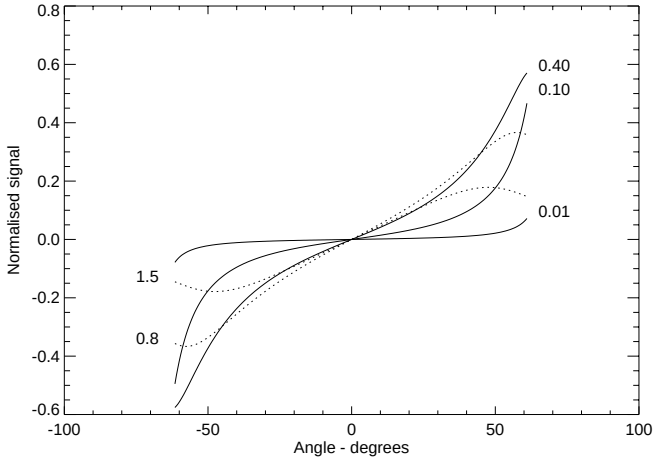

FIG. 1.—Theoretical skydips calculated for the differential signal received by the MISM as a function of zenith angle. Curves are labeled with the value of zenith optical thickness used.

culate the flux that the atmosphere would produce if it were a perfect blackbody. An effective temperature for the atmosphere can then be derived:

$$T_{\rm eff} = \frac{hc}{\lambda k}\left(\ln\left\{\left[\frac{F_\lambda(0)\lambda^3}{(1-e^{-\tau})hc}\right]^{-1} + 1\right\}\right)^{-1}, \quad (3)$$

where h is Planck's constant, k is Boltzmann's constant, and c is speed of light.

When the atmosphere is optically thin, the exponential terms of Equation (2) can be expanded and simplified to give

$$\triangle F(\theta) = A\tau[\sec(\theta + 22.5) - \sec(\theta - 22.5)] . \quad (4)$$

In this case, it is not possible to separately derive the optical depth, τ, and blackbody flux, A—only their product.

To determine the absolute flux from the atmosphere, at least two MISM measurements are required: a reading between the calibration blackbody and a beam at 45° as well as a reading between 45° and zenith. The signal produced by the detector is equal to some responsivity constant (R) multiplied by the difference in the flux between the two positions being observed. (In practice, at least one other measurement is required in order to account for any residual instrumental offset between the two beams of the MISM.) The equations below show the two MISM readings required to calculate the absolute zenith flux.

$$a = R[F(0) - F(45)] , \quad (5)$$

$$b = R[F(45) - F(BB)] , \quad (6)$$

where R is the responsivity of the instrument, $F(\theta)$ is the sky flux at angle θ from the zenith, $F(BB)$ is flux received from the calibration blackbody, and a and b are the output signals of the detector.

By dividing one signal by the other, the detector responsivity term (R) can be removed. If the ratio of the flux at zenith to that at 45° is known, the strength of the zenith flux can be found with respect to that of the calibration blackbody. Using equation (1) above, the ratio of the flux from these two angles is

$$\frac{F(45)}{F(0)} = \frac{1-e^{-\sqrt{2}\tau}}{1-e^{-\tau}} . \quad (7)$$

Using this expression and the signal strengths a and b, a solution for the zenith flux can be found in terms of the ratio of the signals, the flux from the calibration blackbody, and the optical thickness.

$$F(0) = \frac{a}{b} F(BB) \times \left[\left(\frac{1-e^{-\sqrt{2}\tau}}{1-e^{-\tau}}\right) - 1 + \left(\frac{1-e^{-\sqrt{2}\tau}}{1-e^{-\tau}}\right)\frac{a}{b}\right]^{-1} . \quad (8)$$

The simplest solution is when the sky is optically thin and the flux approaches a secant distribution. In this case, $F(45) = \sqrt{2}F(0)$, and is independent of optical depth. Substituting this into the equations above produces the expression

$$F(0) = \frac{a}{b} F(BB)(\sqrt{2} - 1 + \sqrt{2}\tfrac{a}{b})^{-1} . \quad (9)$$

In practice, the optical depth is not known, but this expression is a very good approximation under the conditions we are most interested in—namely, when the sky is optically thin. When the optical depth is a little higher, corrections can be made to the result by choosing an effective temperature ($T_{\rm eff}$) for the atmosphere. The zenith flux can then be written as the product of the blackbody flux at this temperature, $F(T_{\rm eff})$, and emissivity that the optical depth would produce (eq. [1]). Substituting into equation (8) leads to an expression in terms of signals, flux from the blackbody, and flux from the effective temperature and optical depth, as follows:

$$F(0) = F(T_{\rm eff})(1 - e^{-\tau}) , \quad (10)$$

$$\frac{a}{b} F(BB) - F(T_{\rm eff})\left[e^{-\tau} + \frac{a}{b} - e^{-\sqrt{2}\tau}\left(\frac{a}{b} + 1\right)\right] = 0 . \quad (11)$$

By an iterative process, best-fit values for $T_{\rm eff}$, τ, and, hence, $F(0)$ can be derived.

4. RESULTS

4.1. *Skydips*

Figures 2 and 3 show examples of skydips taken by the MISM; that is, the output as the instrument is rotated from one horizon to the other via the zenith. Figure 2 shows skydips at four different wavelengths, taken in clear conditions. Figure 3 shows skydips at the same wavelengths in optically thick, or overcast, conditions.

In the skydips, the signal from the detector is plotted against the zenith angle of the instrument rotator. The zenith angles of the two beams of the MISM are 22°.5 greater than and less than the zenith angle of the rotator. Both MISM beams are facing the sky only for rotator angles between −55° and +45°. Typically, the MISM signal increases monotonically from negative values to positive as the zenith angle increases, depending on which beam is viewing the larger air mass. There are, however, skydips that do not conform to this general shape. At shorter mid-infrared wavelengths, conditions can arise where the optical path length becomes comparable to the height of the atmospheric inversion layer. In this case, the strongest source of thermal emission is the relatively moist air just above the inversion layer, and the emission measured from this layer becomes a strong function of the transmission through the lowest, colder part of the atmosphere. Thermal emission is

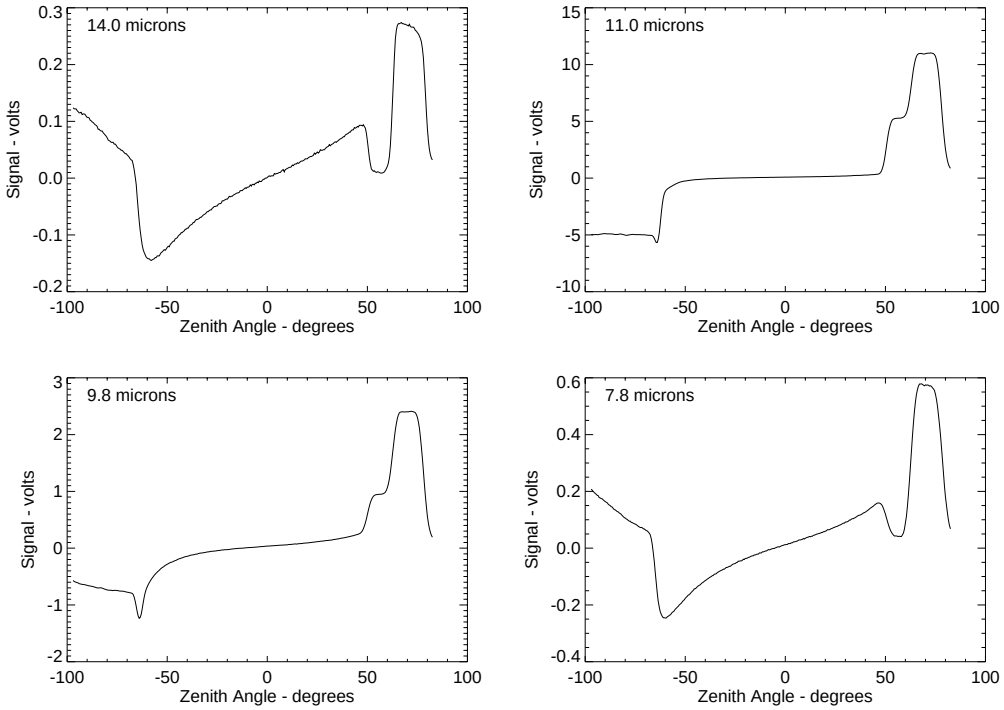

FIG. 2.—Raw skydip data recorded by the MISM at four wavelengths, 14, 11, 9.8, and 7.8 μm, in the mid-infrared. These data were recorded in clear observing conditions on 1998 August 11. The two MISM beams are both facing the sky only for the central portion ($-55^\circ <$ zenith angle $< 45^\circ$) of any raw skydip. At large negative zenith angles, one beam is facing the ice, while at large positive zenith angles, the other beam passes over the calibration blackbody and housing.

then strongest where transmission is greatest, which is at angles close to zenith. This is opposite to the usual case and produces a skydip with a reversed gradient, as in Figure 4.

At angles greater than 50°, the positive beam passes over the calibration blackbody, which is centered at 70°. The blackbody is maintained at a temperature about 30° above ambient so that it is a strong source in the mid-infrared. Consequently, the signal seen when one beam is on the blackbody is the strongest signal on a skydip and dominates the skydip curve, especially at wavelengths in dark portions of the N window. For readings at 55°, one of the beams is passing over the blackbody housing, which can be

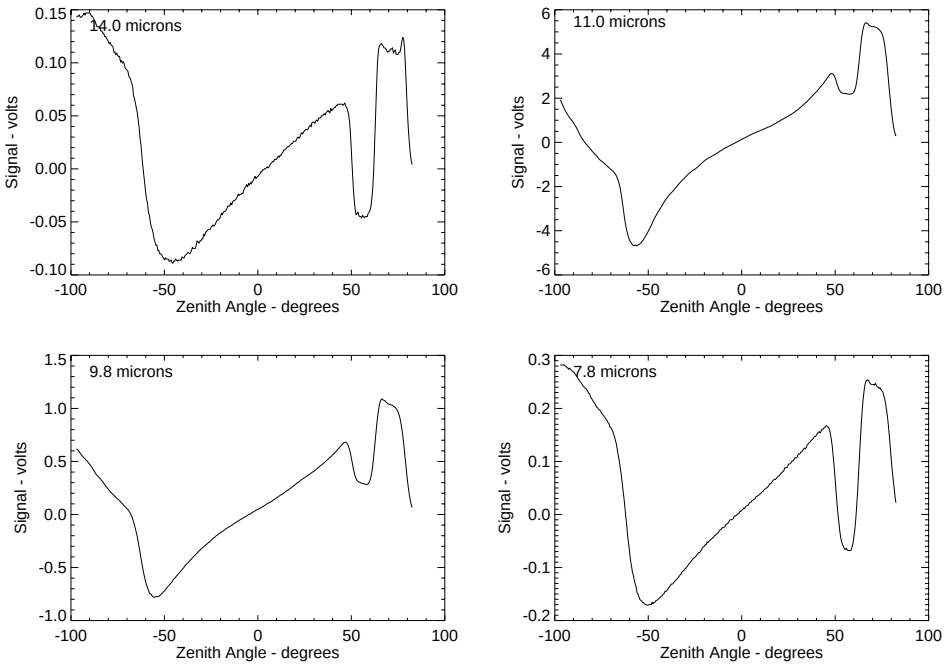

FIG. 3.—More raw skydip data of the same form shown in Fig. 2. These examples were recorded on 1998 August 14, when observing conditions were overcast.

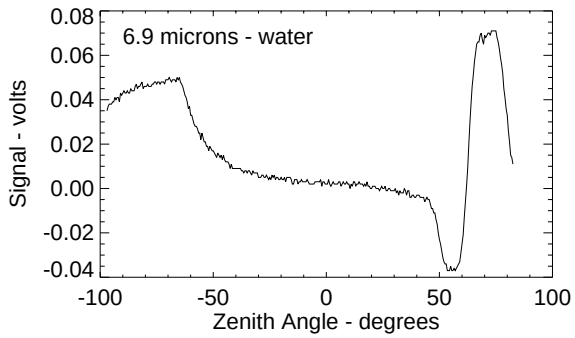

FIG. 4.—Skydip showing conditions when thermal emission is strongest at zenith, demonstrated by a gradient in the skydip that is opposite to that seen in Figs. 2 and 3. This is observed at wavelengths where the atmospheric absorption length is comparable to the height of the inversion layer.

brighter or dimmer than the sky at these wavelengths (in Fig. 3 compare the upper left and lower right panels with the upper right and lower left panels).

At angles less than $-70°$, the negative MISM beam faces into the ice. Depending on the wavelength and the prevailing conditions, the MISM readings show that the sky may be brighter or dimmer than the ground in the mid-infrared.

The wavelengths used in each set of skydips correspond to different emission features to be found in the mid-infrared: carbon dioxide emission (14 μm), a dark portion of the *N* window (10.6–11.3 μm), ozone emission (9.8 μm), and water emission (7.8 μm). There is also a small contribution from methane at 7.8 μm. The wavelengths that show the greatest change in emission with atmospheric conditions are, of course, those within dark portions of the *N* window.

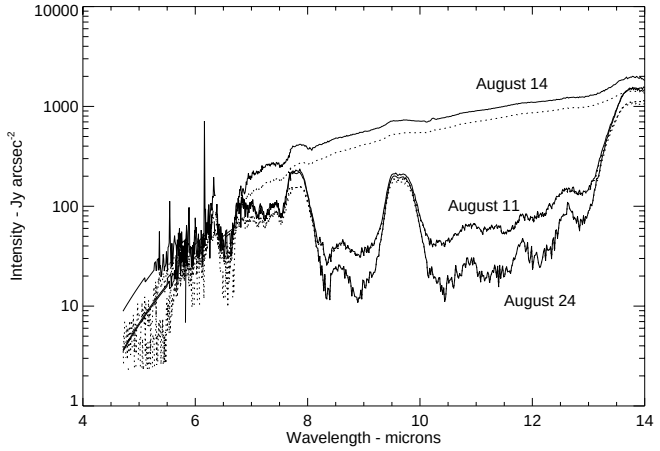

FIG. 5.—Spectra measured with the MISM on days in 1998 August demonstrating different sky conditions. The observing conditions for August 14, 11, and 24 were overcast, clear, and very clear, respectively. Dashed lines correspond to an analysis made assuming a sec θ thermal emission dependence (i.e., optically thin conditions), while the solid line is the result of using a derived optical depth.

The shapes of the skydips recorded are used to make estimates of optical thickness, zenith flux, and effective temperature of the emitting layer. These results are discussed in § 5.

4.2. *Spectra*

Figure 5 shows three spectra derived from data collected from the 11th, 14th, and 24th of August, 1998, demonstrating examples of very clear, clear, and overcast conditions. The dashed lines correspond to an analysis made assuming

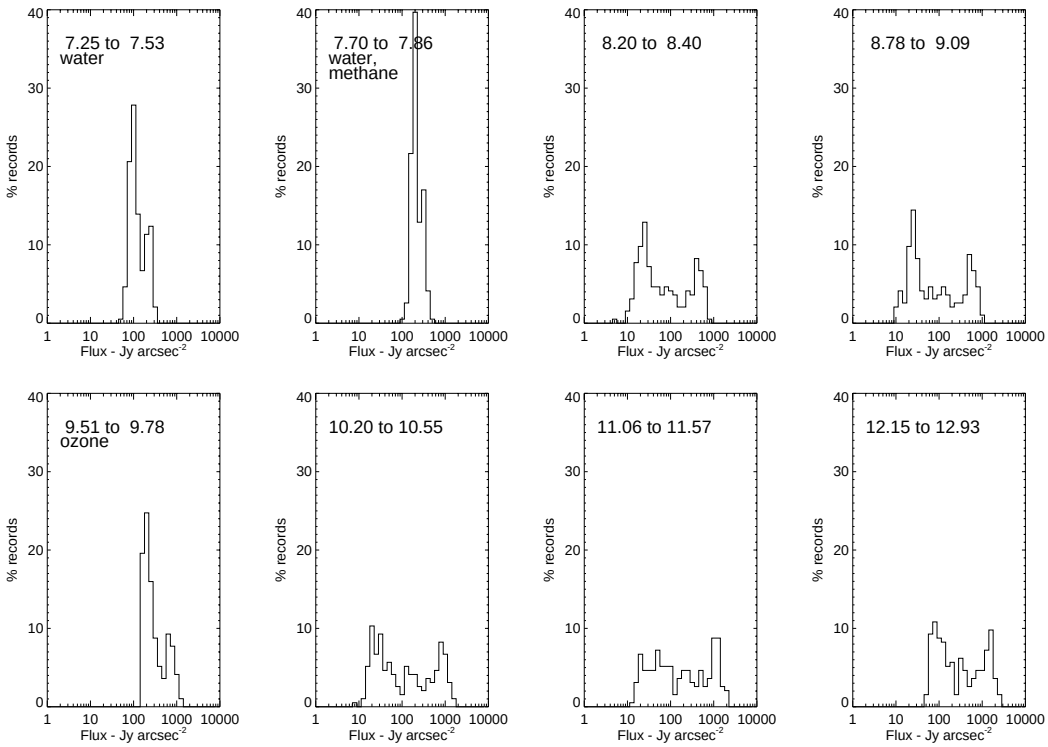

FIG. 6.—Histograms showing the distribution of zenith flux in different mid-infrared bands, as labeled (strong sky emission features are also noted). Fluxes at different wavelengths within the dark portions of the *N* window have a wide range of values, covering 2 orders of magnitude. They also show a bimodal distribution, indicating the sky is typically either clear or overcast and rarely in between at these wavelengths.

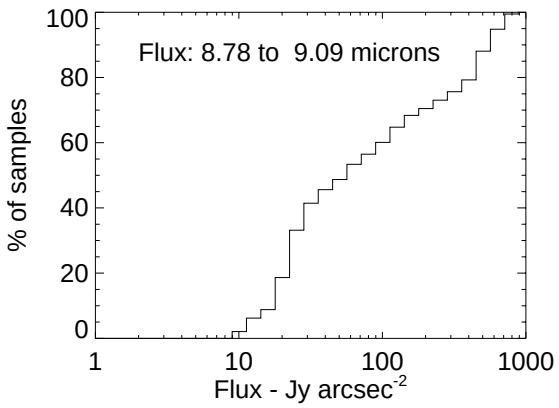

FIG. 7.—Cumulative plot of flux measured in the 8.78–9.09 μm window

a sec θ thermal emission dependence (i.e., optically thin conditions), while the solid line results from using a derived optical depth.

Spectra are generated by scanning through the two circular variable filters, which have resolutions of $\lambda/\triangle\lambda = 74$ and $\lambda/\triangle\lambda = 55$, respectively. Consequently, narrow features, such as the dip in the center of the ozone emission, have not been resolved. The algorithm described in § 3 to determine zenith flux works best for moderately optically thin conditions and breaks down when the sky becomes too optically thick. Wavelengths of 6 μm are near the center of a very optically thick water emission feature; the low values plotted in this region are the result of a failure of the algorithm rather than the discovery of a new atmospheric window.

Emission spectra were calculated regularly throughout the winter of 1998. The histograms in Figure 6 show the distribution of the measured emission within certain wavelength bands from all spectra calculated, including spectra taken during clear and overcast conditions. The only spectra not included are those taken when the sky emission was irregular—either spatially or temporally—thus making calibration impossible, or if there was some malfunction with the instrument, such as trouble with the stepper motors controlling the rotator or the filter wheel. With these criteria, out of a total of 294 instrument runs, 77 were omitted because they could not be calibrated, and 23 were omitted because of technical problems.

Of particular interest are the distributions over the year of emission measured in bands within dark portions of the *N* window. These distributions are bimodal, showing two populations corresponding to clear and overcast conditions, respectively, with a range of values across 2 orders of magnitude. The spectrum from August 14 in Figure 5 falls into the high-emission/overcast population, while August 11 and 24 are part of the low-emission/clear population. Data of August 11 and 24 represent the lowest 40th and 10th percentile, respectively, of all emission recorded. Figure 7 shows a cumulative plot of emission measured in the window from 8.78 to 9.09 μm. The fraction of the total data set indicating clear skies, defined here to be when emission in this band is below 50 Jy arcsec^{-2}, is 50%.

Figure 8 shows the variation in flux over the 1998 winter at several different wavelengths. The bands shown are 7.70–7.86 μm, 9.51–9.78 μm, 8.20–8.40 μm, and 10.20–10.55 μm. These bands correspond to regions that are dominated, respectively, by water and methane emission, ozone emission, and two dark portions of the *N* window. The values

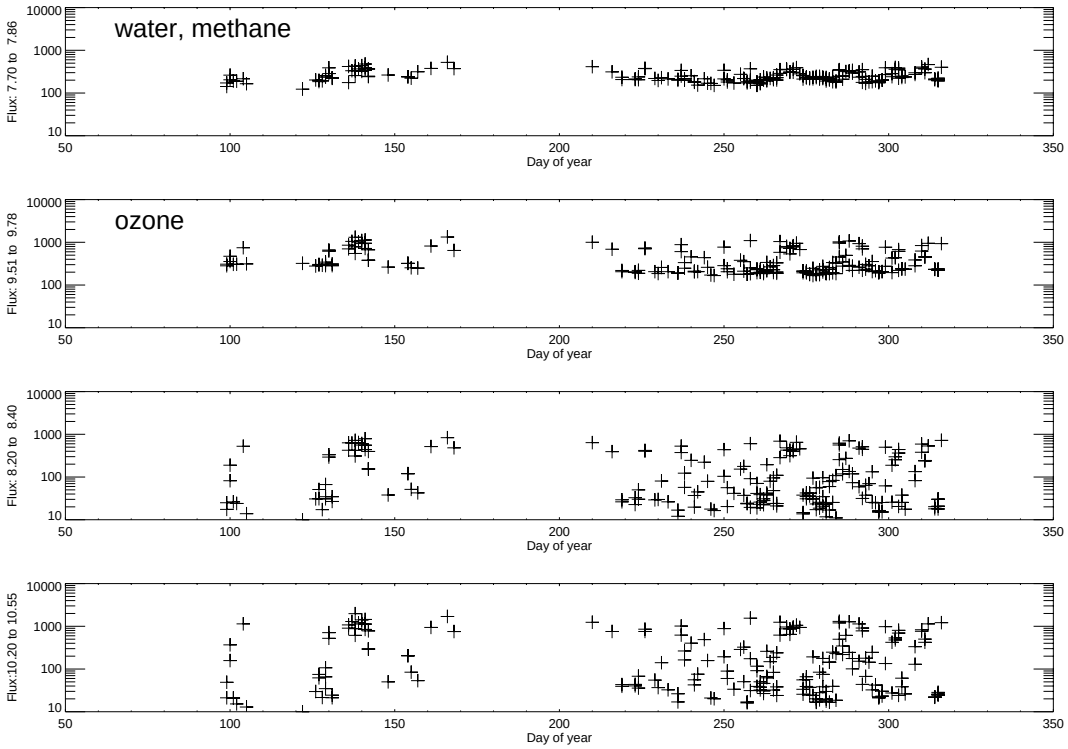

FIG. 8.—Variations in flux over the year for the wavelength ranges 7.70–7.86 μm (water, methane bands), 9.51–9.78 μm (ozone band), 8.20–8.40 μm (dark), and 10.20–10.55 μm (dark).

plotted vary between a minimum emission that depends on both the optical depth and the temperature of the atmosphere and an upper limit determined by the atmospheric temperature alone. There were several occasions during which overcast conditions dominated for several days at a time, in particular around days 140, 270, and 287.

5. ANALYSIS

5.1. *Effective Temperature and Optical Depth*

Table 3 shows the values of the parameters from fitting to the skydips shown in Figures 2 and 3 from August 11 and 14. In clear conditions, the lowest values for optical thickness and emission occur at a wavelength within the clear part of the N window (11.0 μm). However, when the sky is optically very thin, it becomes impossible to separately derive values for the optical depth and atmospheric temperature. Consequently, the values quoted for 11 μm in clear conditions are uncertain. The effective temperatures calculated for the other wavelengths vary, and this can be accounted for in part by emission from different heights and temperatures in the atmosphere. In overcast conditions, the effective temperatures for all wavelengths approach $-40°$C, which matches the temperature of the atmosphere just above the inversion layer.

Figure 9 shows the distribution of results from all successful skydips taken in 1998. Parameter values at 7.8 μm (water and methane) and 14.0 μm (carbon dioxide) show little variation over time because these wavelengths are near major emission features. Temperatures at 14 μm are slightly lower because there is a contribution to the emission from cooler air below the inversion layer. Optical thickness, flux, and temperatures values at 9.8 μm (ozone) have a bimodal distribution corresponding to clear and overcast conditions. The different effective temperatures at 9.8 μm are attributed to emission in the high, cold ozone layer and the relatively warm air just above the inversion layer. Values from 11.0 μm skydips vary widely and are not plotted. As previously noted, the values found for optical thickness and effective temperature for this wavelength are unreliable in clear conditions because the two parameters cannot be separated.

Some systematic variation in the optical thickness and emission level was observed in the skydips at 9.8 μm, which is within the ozone emission feature. Figure 10 shows the variation of optical thickness at this wavelength in 1998, as measured in clear conditions only. There is a decrease over the whole of the winter (bear in mind that the actual optical thickness could in fact be lower than the minimum values plotted). The time of year when the optical thickness starts to increase, DOY 300, coincides with the collapse of the ozone hole. It also appears that the cold temperature over the winter reduces the emission from the ozone layer.

5.2. *Modeling*

Theoretical mid-infrared emission spectra were calculated with the "Modtran" modeling package (AFRL/VSBM).[1] Modtran calculates transmission and emission of the atmosphere at wavelengths from the optical to the far-infrared. Within Modtran it is possible to define the atmospheric profile used to perform these calculations. Several default profiles are available based on atmospheric profiles in common geographic locations; however, it is also possible to create user-defined profiles.

Data from meteorological balloon launches from the South Pole were used to define the atmospheric profiles we used with Modtran. Pressure, temperature, and relative humidity profiles are measured daily, and an ozone balloon is released once a week (CMDL/NOAA).[2] Figure 11 shows the pressure, temperature, and humidity recorded on August 11 and 14, corresponding to days when conditions were clear and overcast, as seen in the MISM skydips and spectra of Figures 2, 3, and 5. The main difference in these profiles is an increased surface temperature and an increase in humidity above the inversion layer during the overcast conditions of August 14.

The total water-vapor content of the atmosphere for August 11 and 14, as calculated by Modtran from our data, is 150 and 290 μm of precipitable water, respectively. These values compare well with the upper 25th percentile and top 75th percentile of values determined previously from 1992 radiosonde data (Chamberlin & Bally 1995). However, when thermal emission is calculated for the profiles from these two days, the difference in water vapor causes no perceptible change in the mid-infrared flux. Model spectra for both days were found to give emission levels lower than those observed, even in the "clear" conditions of August 11. Fluxes measured by the MISM at 11 μm for August 11 and 14 were 60 and 1000 Jy arcsec^{-2}, respectively, whereas the modeled flux for both 150 and 290 μm of precipitable water vapor is only 10 Jy arcsec^{-2}.

[1] Air Force Research Laboratory (AFRL/VSBM), 29 Randolph Road, Hanscom AFB, MA 01731-3010; http://www-vsbm.plh.af.mil/soft/modtran.html.

[2] Climate Monitoring and Diagnostics Laboratory (CMDL), NOAA, 325 Broadway R/E/CG, Boulder, CO 80303; http://www.cmdl.noaa.gov/spo/.

TABLE 3

DERIVED PARAMETERS FROM SKYDIPS ON AUGUST 11 AND 14[a]

	AUGUST 11			AUGUST 14		
WAVELENGTH (μm)	Optical Thickness	Zenith Intensity Jy arcsec^{-2}	Effective Temperature (K)	Optical Thickness	Zenith Intensity Jy arcsec^{-2}	Effective Temperature (K)
7.8 (H_2O).....	0.57	210	223	0.93	420	233
9.8 (O_3).....	0.18	150	210	0.69	890	232
11.0 (clear).....	0.015	44	239	0.45	970	236
14.0 (CO_2).....	0.71	1600	220	1.40	2700	226

[a] Fitted values from August 11 and 14 represent typical values found in clear and overcast days, respectively. For the 11 μm data on August 11 the effective temperature is that required to produce the observed zenith flux for an emissivity of 1.5%, as derived for the atmospheric model described in § 5.2 (see discussion in text). Histograms presenting distributions of values found from fitting to all the suitable skydips from 1998 are shown in Fig. 9.

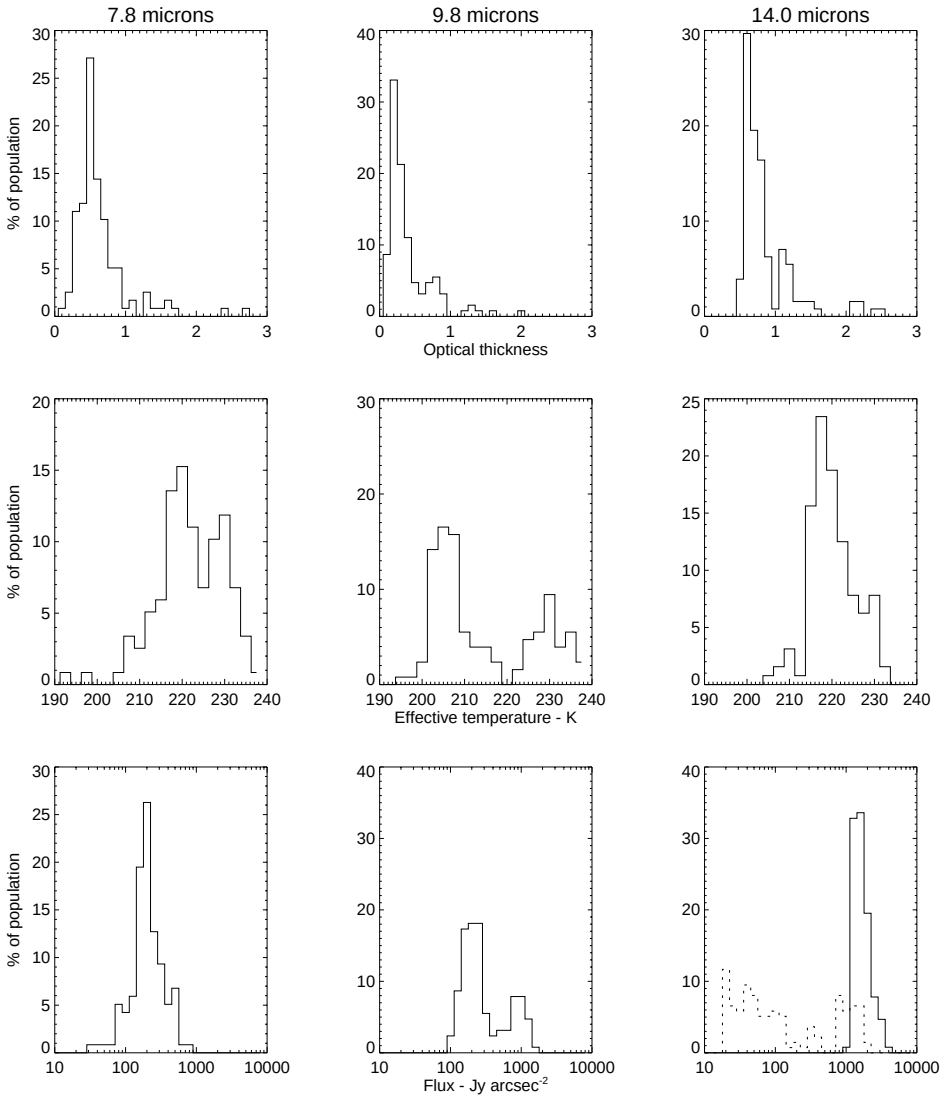

FIG. 9.—Histograms of the parameter values for optical thickness, effective temperature of the emitting atmosphere and sky flux, fitted to skydips taken at 7.8 μm (H_2O), 9.8 μm (O_3), and 14.0 μm (CO_2) during 1998. The histogram for the 11 μm (clear) sky flux is shown as a dashed line on the 14 μm plot (the determination of optical depth and temperature is degenerate at 11 μm in clear conditions—see text).

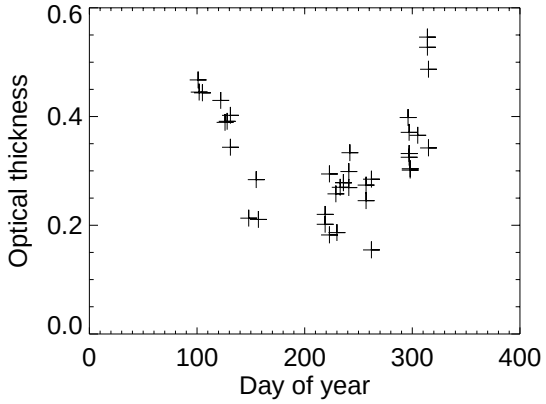

FIG. 10.—Variation in the optical thickness fitted to 9.8 μm ozone emission taken in clear conditions over the 1998 winter, indicating a decrease over winter and into spring. The increase from day 300 coincides with the start of the collapse of the ozone hole.

This difference between modeled and measured emission can be ascribed to emission from "aerosols." Of all the different aerosol types available for use by Modtran, "radiative fog" was found to produce a mid-infrared emission spectrum that was most similar to the spectra measured by the MISM. While these models do not provide any real clues as to the nature of the aerosols over the South Pole (which would be expected to be predominantly ice particles), they do suggest that aerosols are the main contributors to the mid-infrared background in the cleanest parts of the *N* window. Ever-present low levels of emission from "ice particles" or "blowing snow" have been noted already by Van Allen, Murcray, & Liu (1996) from atmospheric measurements they made at the South Pole with a Fourier transform spectrometer.

The second main aerosol parameter, visibility, is used to define the amount of aerosol in the atmosphere. Figure 12 shows different mid-infrared emission spectra modeled with

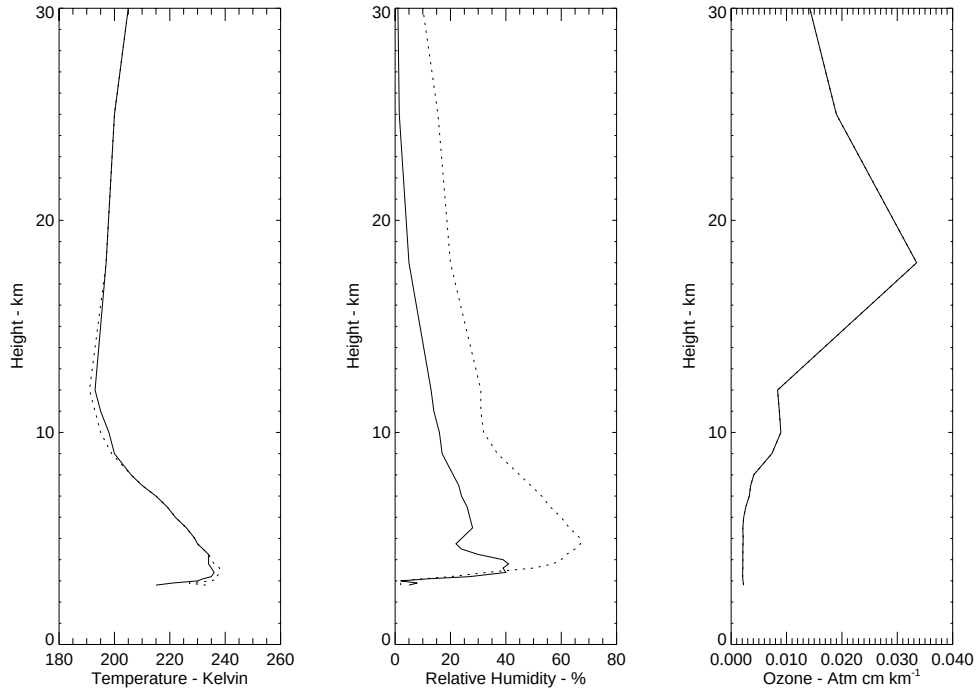

FIG. 11.—Profiles of the temperature, relative humidity, and ozone, as measured by weather balloons from the South Pole (CMDL/NOAO; see fn. 2 in text). The solid and dotted profiles were measured on August 11 and 14, respectively, corresponding to clear and overcast conditions, respectively.

the same temperature and humidity profile (based on data from August 11) with varying visibilities of "radiative fog" aerosols. Spectra from clear and overcast days, like the curves from August 11 and 14 shown in Figure 5, correspond well to the emission curves in Figure 12 with visibilities of 50 and 0.5 km, respectively.

These results suggest that in the clearest conditions at the South Pole, the thermal emission in the *N* window from the atmosphere is limited not by the remaining water vapor but by aerosols. At still higher sites on the antarctic plateau, where lower wind speeds are expected to result in lower amounts of wind-borne ice crystals and the turbulent atmospheric boundary layer is expected to be thinner, it is possible that the mid-infrared sky will be substantially darker again than at the South Pole.

Comparisons with results using the mid-infrared camera NIMPOL in clear conditions over Canberra, Australia, and at Mauna Kea (Smith & Harper 1998) are shown in Figure 13. The South Pole fluxes are typically an order of magnitude lower than even those at Mauna Kea.

Using the atmospheric model that is found to best match our data in the mid-infrared, we can extend the calculations into the near-infrared and far-infrared to produce the plots of emission and transmission shown in Figures 14 and 15. (Note that this model does not include the hydroxyl airglow emission that dominates the sky at wavelengths shorter than 2.3 μm.) In the near-infrared, between 2.4 and 4 μm, these models closely match the observed spectra obtained by Phillips et al. (1999). Selected windows are available from 17 to 30 μm in the mid-infrared where observations will be significantly improved compared to temperate latitude sites. It is also apparent that new atmospheric windows in the

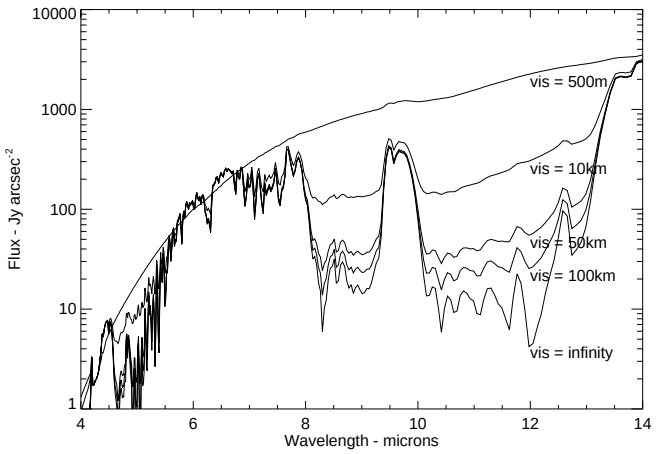

FIG. 12.—Model mid-infrared spectra for different levels of "visibility" of fog aerosols (from 500 m to completely clear) in winter over the South Pole. These can be compared to the observed sky spectra in Fig. 5.

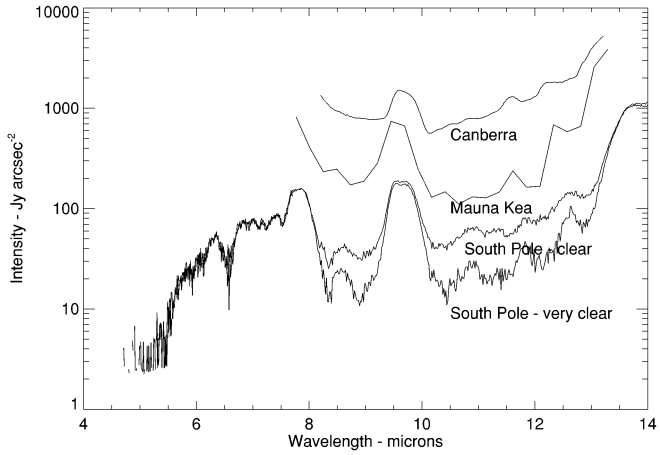

FIG. 13.—Comparison of emission spectra taken in clear conditions at Canberra and Mauna Kea (Smith & Harper 1998) with data from the South Pole (this work).

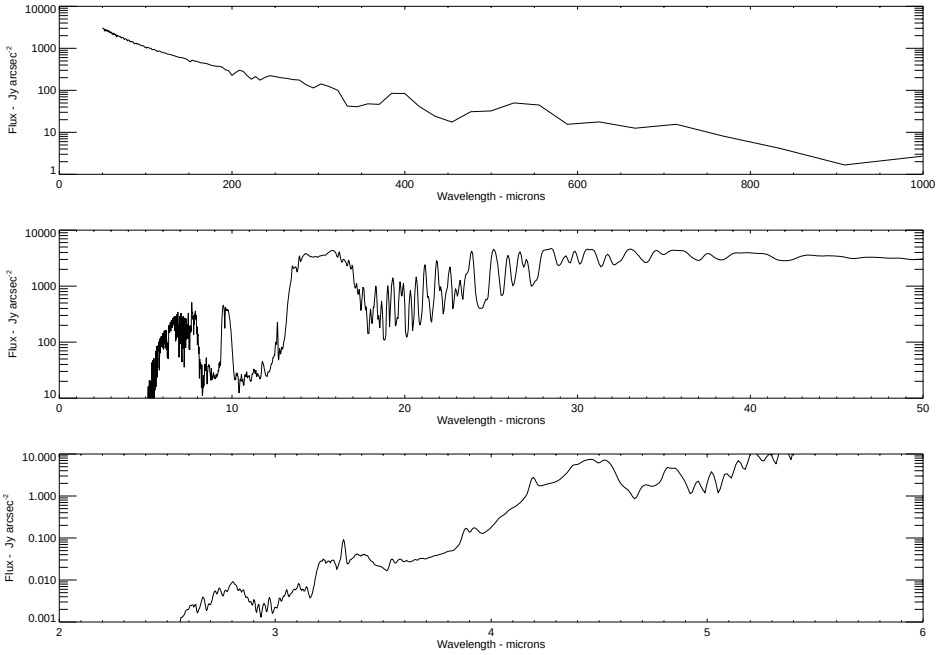

FIG. 14.—Calculated sky emission flux in Jy arcsec^{-2}, from the near- to far-infrared using the atmospheric model that best matches the mid-infrared emission over the South Pole under "very clear" conditions. Note that this model does not include the OH airglow emission shortward of 2.3 μm.

far-infrared will become accessible from the South Pole, particularly at around 200 μm and from 225 to 245 μm. The 200 μm window is expected to be especially important, as it should make the 203.5 μm fine-structure line of [N II] accessible to ground-based observation. This line is an important coolant of the interstellar medium but, until now, has been observable only from space or from stratospheric observatories. Finally, the submillimeter windows at 350 and 450 μm are particularly clear.

6. CONCLUSION

During the austral winter of 1998, the MISM took data at the South Pole for a total of 140 days. These data have been analyzed to show that:

1. The sky was clear for 50% of those occasions for which data were available.
2. The typical flux from 8.78 to 9.09 μm during those clear days was 20 Jy arcsec^{-2}.

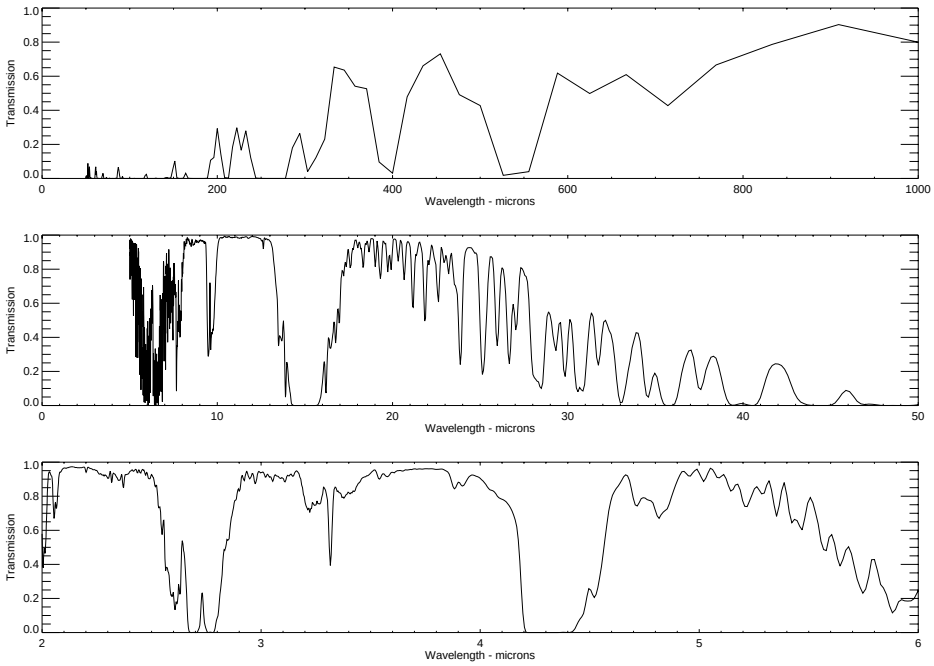

FIG. 15.—Calculated atmospheric transmission from the near- to far-infrared using the atmospheric model that best matches the mid-infrared emission over the South Pole under "very clear" conditions.

3. These flux values are about an order of magnitude lower than typical values at Mauna Kea.

4. The lowest flux recorded in the 8.78–9.09 μm window was 10 Jy arcsec^{-2}.

5. The lowest flux in the N window is set not by residual water vapor but by "aerosols."

6. The strength of the ozone emission feature at 9.8 μm is seen to vary throughout the year in a way consistent with the known variation in stratospheric ozone over the South Pole.

7. Derived values for the column of precipitable water vapor through the atmosphere are consistent with those measured via other techniques.

8. The values of water vapor and atmospheric aerosol content derived from the MISM data can be used to model the atmospheric transmission to both shorter and longer wavelengths. New windows for ground-based observation are apparent.

We thank Max Boccas and Antony Schinckel for their help with the development and deployment of the MISM instrument and the Electronics and Mechanical Workshops at the University of New South Wales for their dedicated assistance. We are also indebted to Craig Smith for helpful discussions and to Robert Schwartz for keeping the MISM alive during the antarctic winter after the second failure of the AASTO power system. This research is supported by the Australian Research Council and DIST, together with the NSF through their support of the Center for Astrophysical Research in Antarctica under grant OPP 89-20223.

REFERENCES

Ashley, M. C. B., Burton, M. G., Storey, J. W. V., Lloyd, J. P., Bally, J., Briggs, J. W., & Harper, D. A. 1996, PASP, 108, 721
Chamberlin, R., & Bally, J. 1995, Int. J. Infrared Millimeter Waves, 16, 907
Fowler, A. M., et al. 1998, Proc. SPIE, 3354, 1170
Low, F. J., & Rieke, G. H. 1974, in Methods of Experimental Physics 12, ed. N. Carleton (New York: Academic), 447
Nguyen, H. T., Rauscher, B. J., Severson, S. A., Hereld, M., Harper, D. A., Loewenstein, R. F., Mrozek, F., & Pernic, R. J. 1996, PASP, 108, 718
Phillips, M. A., Burton, M. G., Ashley, M. C. B., Storey, J. W. V., Lloyd, J. P., Harper, D. A., & Bally, J. 1999, ApJ, 527, 1009
Smith, C. H., & Harper, D. A. 1998, PASP, 110, 747
Storey, J. W. V., Ashley, M. C. B., & Burton, M. G. 1996, Publ. Astron. Soc. Australia, 13, 35
Storey, J. W. V. 1998, in ASP Conf. Series 141, Astrophysics from Antarctica, ed. G. Novak & R. H. Landsberg (San Francisco: ASP), 313
Storey, J. W. V., Ashley, M. C. B., Boccas, M., Phillips, M. A., & Schinckel, A. E. T. 1999, PASP, 111, 765
Van Allen, R., Murcray, F. J., & Liu, X. 1996, Appl. Opt., 35, 1523